New methodology of dynamical material response of dissimilar FSWed Al alloy joint under high strain rate laser shock loading

Mohammad Ayad [a], Lucas Lapostolle [a], Alexandre Rondepierre [a,b], Corentin Le Bras [a,c], Selen Ünaldi [a], Črtomir Donik [d], Damjan Klobčar [e], Laurent Berthe [a], Uroš Trdan [a,e,*]

[a] *PIMM, UMR8006 ENSAM, CNRS, CNAM, 151 bd de l'Hôpital, 75013 Paris, France*
[b] *THALES LAS France, 78990 Elancourt, France*
[c] *Airbus Operation S.A.S, 316 route de Bayonne-B.P.D4101, CEDEX 9, F-31060 Toulouse (C.L.B), France*
[d] *Institute of Metals and Technology, Lepi pot 11, 1000 Ljubljana, Slovenia*
[e] *Faculty of Mechanical Engineering, University of Ljubljana, Aškerčeva cesta 6, 1000 Ljubljana, Slovenia*

HIGHLIGHTS

- New methodology of material characterization in high strain rate regime.
- Successful distinction between material planes and its properties.
- Perfect correlation between grain size, residual stresses and J-C parameters.
- Prediction of material behaviour under dynamic loading.

GRAPHICAL ABSTRACT
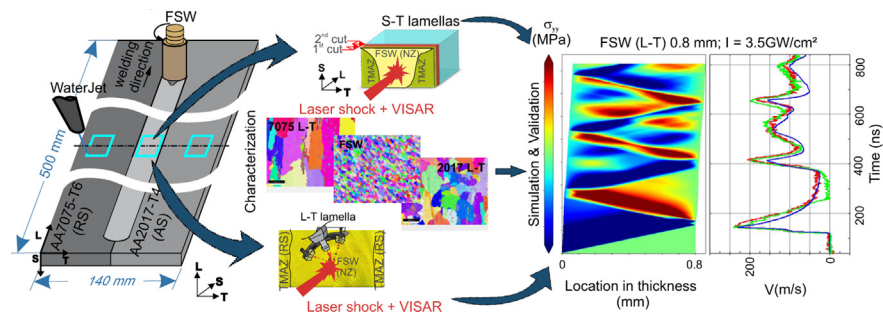
ARTICLE INFO

ABSTRACT

This paper presents an innovative methodology of material characterization under high strain rate (order of $10^7 s^{-1}$) laser shock loading coupled with microstructural and mechanical material features. To that scope, experimental and simulation analyses have been conducted for Al alloys (AA7075-T6 and AA2017-T4) and dissimilar Friction Stir Welded (FSWed) AA7075-AA2017 joint, under shock pressure of 4.5 GPa (laser power density of 3.5 GW/cm^2). In order to perform proper in-depth material model simulation of these alloys and dissimilar pairs, Johnson–Cook (J-C) material model has been coupled with Grüneisen equation of state using the non-linear explicit code LS-DYNA. For the first time, we provided a way to differentiate between material behaviour in the cross-section and the in-plane rolling and welding direction. What is more, we have provided the link between microstructural features and mechanical properties such as microhardness, residual stresses and the identified material parameters. By achieving this goal, the bigger difference between studied planes was confirmed for strain hardening modulus, strain hardening exponent and strain rate sensitivity parameters. Obtained results and proposed methodology indicate high potential to predict material properties and behaviour of dynamically stressed parts and at the same time can be used for optimization of LSP process.

1. Introduction

The growth in air transport is altering the atmosphere compositions by causing an increase in greenhouse gas (GHG) and increas-

* Corresponding author.
 E-mail address: uros.trdan@fs.uni-lj.si (U. Trdan).

ing atmospheric pollution. EU ambition is towards Climate-Neutral Aviation, which needs the contributions of several innovation technologies (fuel consumption efficiency, weight reduction and coat/-paint stripping [1]. One of the interest in the domain is the structure weight reduction [2,3], using light-weight parts made of dissimilar materials [4–8], which influences directly the fuel consumption and subsequently the pollutant emission. Advanced manufacturing processes provide methods to reduce structure weight but they should always follow the safety standards and require less energy consumption for repairing and maintenance [9,10].

High-strength aluminum (Al) alloys are important constructional materials, mainly because of their lightweight, high specific strength, good damage tolerance ability, good workability, good electrical conductivity and corrosion resistance in non-aggressive environments [11–13]. Hence, 2xxx and 7xxx high-strength Al alloys are widely used for highly stressed structural applications in aerospace and aircraft industries [14]. However, joining of dissimilar 2xxx and 7xxx Al alloys is rather demanding due to the numerous intermetallic phases' (S phase (Al_2CuMg), θ phase (Al_2Cu), Mg_2Si, Al_7Cu_2Fe, $(Al, Cu)_6(Fe, Cu)$, T phase ($Al_{20}Cu_2Mn_3$), Al_3Fe, $Al_4Cu_2Mg_8Si_7$, AlCuFeMnSi and others) [15–18], different melting temperatures and the formation of eutectic and fragile intermetallic phases in the fusion zone [19]. Hence, "heavy-weight" riveting is predominately used since fusion welding of such Al alloys led to insufficient welds with solidification (hot) cracks, porosity, segregation, brittle secondary intermetallic formation and undesired residual stresses [5,20].

One of the innovative aeronautical material processes is the "solid-state" Friction Stir Welding (FSW), invented by TWI in Cambridge, England, for joining Al alloys [21]. Eclipse Aviation made 128 m of FSWed joints to replace 7000 rivets. What is more, the elimination of holes and rivets provides a lighter aircraft, yet three times stronger than a traditional riveted airframe as has been approved by the Federal Aviation Administration (FFA). Moreover, with FSW no protective gas or feed material is needed and the energy input is significantly lower compared to the fusion welding processes, which reduces harmful gas emission [22,23] and eliminates several defects associated with melting and re-solidification. Due to the lower temperature input, the welds minimally deform with a small geometric deviation, whereas due to the effect of dynamic recrystallization (DRX) crystal grains in the nugget zone (NZ) are isotropic, homogeneous and considerably smaller than in the base material of high-strength precipitation hardened Al alloys [24].

Different tests have been carried out on dissimilar Al alloy to evaluate the joining influence on material mechanical properties [18,25–28]. Optimization of the joined material properties (welded material) demands a detailed understanding and descriptive modeling of the FSW process. Ahmed et al. [29] developed a mathematical model to predict the heat generation during the welding process. The authors validate their model with experimental measurement on AA1050 by taking into account different pin geometries. Simoncini et al. [30] also developed different metamodels using a series of statistical methods, which have been validated with experimental tests. The authors used their validated algorithms to optimize the FSW parameters in order to enhance the mechanical performance of the joint. The influence of the welding parameters such as the traverse speed (welding speed), rotational speed and the number of passes on the mechanical properties of the formed material has been analyzed by many authors [31,32].

What is more, FSW process parameters have been coupled with the welded material properties in Grujicic et al. [33], where the authors modify the original Johnson–Cook material model to take into account the microstructural modification in the welded mate-

rial during the FSW. The authors provide a new material model which can be used to optimize the welding process to obtain optimum weld performance. Vimalraj et al. [30] proved that incorporating nanoparticles plays a crucial role in the microstructural properties where authors investigated the influence of size, type and amount of nanoparticles on the microstructural formation and joint properties. In order to decrease manufacturing time one can increase the welding speed or increase the pin tool diameter, but the influence on the joint strength should be taken into account. Dimopoulos et al. [32] investigated the influence of welding speed, tool pin diameter and rotation speed on joint strength. The authors proved that maximum strength using a 4 mm pin diameter could be obtained using 110 mm/min and 1500 rpm welding speed and rotational speed accordingly. What is more, the authors proved that higher strength can be obtained using a larger pin diameter, but this does not hold true in the case of 1000 rpm where the mechanical strength of the joint is independent of the pin diameter. Despite the optimization of the FSW process, the fatigue life and strength of welded dissimilar Al joints should be enhanced. Therefore, Laser Shock Peening (LSP) has been applied [34–36].

Due to the narrow optimal engineering window associated with numerous LSP parameters (power density, focal spot, overlapping, pulse duration, treatment pattern and others), it is crucial to optimize the LSP process. Hence, numerical simulations are necessary before practical experimental applications. This will save cost and time. Apart from the static tensile tests, which could identify the joint strength, the material's ability to deform elastically and plastically without breaking at high-strain rate is crucial. The Plastic deformation of polycrystalline materials at high-strain rate depends on the material defect kinetic and its interaction with the microstructures [37,38]. Peyre et al. [39] investigated the high strain rate behavior of welded Al alloys. Authors proved that FSWed Al alloys exhibit high strain-rate sensitivity, by comparing their numerical and experimental measurements of the shock wave attenuation and elastic precursor amplitude. However, their material model has been validated only on the first shock period and for one material configuration, i.e. cross-section (S-T) plane of the investigated material. Up to now, no high accuracy validation of long-time laser shock propagation (multi-period of the wave) through AA7075-T6 and AA2017-T4, nor FSWed dissimilar AA7075-AA2017 joint has been reported. What is more, wave propagation produced by a laser impact on the base Al alloys and on the FSWed dissimilar joint in the in-plane (L-T) direction has not yet been investigated.

Hence, in the current work, the high accurate methodology from Ayad et al. [40] has been used for material model characterization of the dissimilar AA7075-AA2017 FSWed joint and base materials, taking into account different microstructures in specific rolling directions. Eventually, numerical and experimental data were combined to identify material model behavior under high strain rate. For the first time, microstructural features, mechanical state of the studied materials/regions and planes of dissimilar FSWed joint coupled with experimental long-time Back Face Velocity (BFV) measurement have been investigated. Moreover, the adjustment of the material model to reproduce the experimental BFV measurements has been provided and correlated with materials' microstructural and mechanical features.

2. Experimental setup

2.1. Materials and FSW process

In the present investigation dissimilar butt joints were produced by a single-sided FSW process, using AA7075-T6 and

M. Ayad, L. Lapostolle, A. Rondepierre et al.

AA2017-T4 rectangular plates of 500 mm (length)×70 mm (width)×10 mm (thickness), with the following chemical compositions (in wt.%); i.e. 5.9 Zn, 2.8 Mg, 1.6 Cu, 0.18 Cr, 0.12 Fe, 0.08 Si, 0.03 Mn, 0.10 (others), Al balance and 4.06 Cu, 0.74 Mg, 0.42 Mn, 0.42 Si, 0.32 Fe, 0.07 (others), Al balance, respectively. Prior to FSW process, all plates were thoroughly degreased with acetone and ethanol and hydraulically clamped on a bucking plate. Welding was performed along the longitudinal (L) rolling direction using the following, pre-determined parameters, i.e. constant rotation per feed of 20 rpcm, weld force of 38 kN, tool tilt angle was 1°, contra-clockwise (CCW) rotation with a tool offset of 1 mm toward the retreating (AA7075-T6) side. A cylindrical threaded tool with a pin and shoulder diameter of 9 mm and 25 mm, has been used. In this study, FSW parameters were chosen based on a preliminary tests, visual appearance, bending and tensile results and microstructural examination (results not presented herein).

The (S-T) and (L-T) lamellas were cut out from the FSWed plate using a waterjet process along the longitudinal (L) and transverse (T) rolling direction to obtain 20×20×10 mm³ blocks. Then we have sectioned the blocks using wire electric discharge machining (EDM) in the S-T direction and L-T direction to obtain ∽0.8 and ∽1.2 mm thick lamellas (Fig. 1). For each set of lamellas (plane & thickness), three samples were prepared for further experimental analyses; (i) laser shock wave loading and propagation monitoring using Velocity Interferometer System for Any Reflector (VISAR), (ii) microstructural observations and (iii) XRD residual stress and microhardness measurements. Prior to laser shock experiments all the samples were thoroughly degreased with alcohol, acetone and rinsed with deionized water. Mechanical and material model properties of these materials has been collected from different literature works [41–44] as summarized in Tables 1,2.

2.2. Microstructural studies

Investigation of microstructural features of base materials (BMs) and FSWed joint for S-T and L-T plane, respectively, were conducted using optical/digital microscopy (DM) and scanning electron microscopy (SEM). Prior to DM, the samples were successively grinded, polished and anodized in Barker's reagent (97.5 mL H_2O, 2.5 mL (HBF_4)) at U = 23 V for approximately 2 min to reveal the grain structure. Following that, the microstructure images were observed using a DM Keyence VHX-600 under polarized light configuration and stitched together to obtain a 2D presentation of the complete FSW region of investigated samples in the S-T and L-T

planes, respectively. SEM analyses were performed using a Carl Zeiss FIB-SEM CrossBeam 550, equipped with a Hikari super EBSD Camera and Octane Elite for EDS measurements, both from EDAX. An acceleration voltage of 15 kV at 2 – 5 nA was used for SE images. In order to obtain quantitative information crystallographic information about the texture and grain size, the Electron Back-Scatter Diffraction (EBSD) was employed [45]. For the EBSD measurements, the samples were tilted for 70° and scanned with an acceleration voltage of 15 kV and a probe current up to 10 nA was used. A larger area on different parts of FSW was examined and the most representative elements were chosen for presentation. All samples for SEM analyses techniques were mechanically polished with 1 μm diamond suspension, followed by 10 min of OPS (SiO_2 nanoparticles) finishing.

2.3. Residual stress determination and microhardness

In order to investigate the effect of the FSW process on the mechanical state and to correlate it with the microstructure and material model characteristics under high strain rate deformations, residual stresses (RS) were determined in the center of the sample/lamella, i.e. region of LSP shock wave impact (see Fig. 1). Measurements were carried out by a Proto iXRD system according to the $sin^2\psi$ method with a focused X-ray beam of 2 mm, using the Al {311} X-ray diffraction (XRD) peak of Cr-Kα X-rays (2.291 Å) located at 2θ = 139°. The side inclination method with 9 β angles and 5° oscillation was used for each measurement point and the Gaussian profile fitting and X-ray elastic constant $\frac{1}{2}S_2^{311} = 19.54 \times 10^{-6}\,MPa^{-1}$ was applied for the residual stress calculation. Residual stresses were determined along the primary shock wave loading direction, i.e. L and S direction for the S-T and L-T lamellas, respectively. Microhardness measurements were conducted with a Vickers microhardness tester a Zwick/Roell ZHU 2.5 at 300 g load with a dwell time of 12 s, with an increment of 500 μm between each specific indentation. For the comparison with the RS, the microhardness measurements were performed in-line at the center of each specific lamella, i.e. different regions (BMs and NZ) and planes (L-T and S-T). On average, 10 measurements were performed for each specific region and plane for the BMs and 20 measurements for the FSW NZ, respectively. Then the average and the standard deviation were calculated in order to obtain reproducibility of the results. In addition, to correlate the mechanical properties with the microstructural features along the weld zone, three separate microhardness measurements were
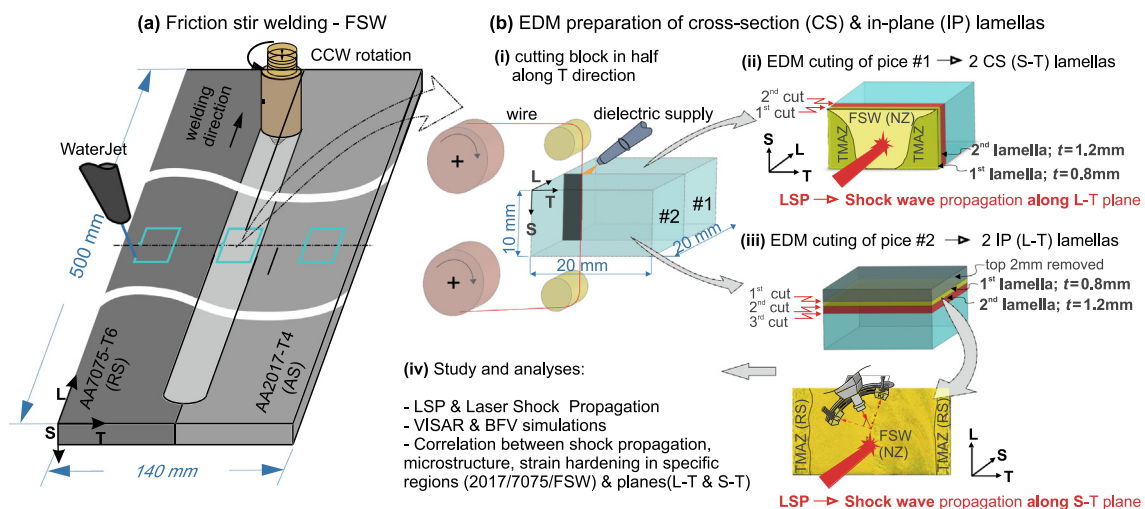

Fig. 1. Schematic presentation of (a) FSW process and (b) EDM preparation of CS (S-T) and IP (L-T) lamellas.

Table 1

Mechanical properties for AA7075-T6 and AA2017-T4 [43].

Material	$\rho(\text{kg/m}^3)$	$G(\text{GPa})$	$C_p(\text{J/g}°\text{C})$	$T_m(°\text{C})$	$T_0(°\text{C})$
AA7075-T6	2700	26.9	0.96	477–635	25
AA2017-T4	2790	27	0.88	513–640	25

Table 2

Johnshon-Cook parameters of AA7075-T6 [41] and AA2017-T4 [44] and Grüneisen parameters for AA7075-T6 [42] and for AA2017-T4 [44].

Material	$A(\text{MPa})$	$B(\text{MPa})$	C	n	$C_0(\text{m/s})$	S_1	γ_0
AA7075-T6	473	210	0.033	0.3813	5386	1.339	1.97
AA2017-T4	270	426	0.015	0.34	5379	1.29	2

made across the middle of joint in the L-T and S-T direction using an increment of 0.5 mm.

2.4. Used laser systems and optical setup

Laser shock experiments were performed using a GAIA laser system (made by Thales, France). This laser is based on a MOPA (Master Oscillator Power Amplifier) configuration: a Nd:YAG crystal, flashlamp-pumped, is operated with a pockels cell (active Q-Switching) in order to generate a gaussian laser pulse (FWHM: 7.2 ns). Then, the seed laser pulse goes through 3 amplifiers (also made of Nd:YAG crystals pumped by flashlamps) in order to reach a high output energy of 12 J in the infrared. Moreover, a nonlinear crystal (KDP) is used to convert the laser pulse into the green visible wavelength (532 nm), with output energy of 7 J. Since two separate beams of 7 J are created, the total laser energy can reach 14 J. This laser system can be operated both or in single-pulse mode with a repetition rate of 2 Hz. The spatial profile of the beam is smoothened (top-hat profile) using a DOE (Diffractive Optical Element) and a converging focal lens to obtain a spot size of 3 mm. A Basler-ac camera has been used to measure the laser spot size profile irradiating the metal target before each set of experiments.

2.5. Velocity measurement with VISAR system

Measurements of target behavior under laser shock have been performed using a VISAR (Velocity Interferometer System for Any Reflector) to obtain a time-resolved (ns range) measurement of the Back Face Velocity (BFV). Similarly to a radar system, a VISAR uses the wavelength-shift of its probe beam (a single longitudinal mode Verdi laser made by Coherent) by Doppler-Fizeau effect, because of the acceleration experienced at the rear-surface and induced by the shock wave. This shift is acquired in a Michelson-like interferometer to obtain accurate measurements. A schematic presentation of the working principle of the VISAR is illustrated in Fig. 2c.

3. Mechanical modeling

In this study, we have used the explicit solver LS-DYNA which has the ability to reproduce the dynamical behavior of Al alloys under high strain rate laser shock loading [40]. In the sequel, we show the developed mesh (Section 3.1) and material model with the associated equation of state (Sections 3.2 and 3.3) used in this study.

3.1. Mesh and geometry

Following previous work [40], we have used a 2D axisymmetric model to simulate the dynamical behavior of the studied Al alloys. The 2D mesh with 1.85 μm×4 μm element size has been used to generate the axisymmetric sample based on the revolution symmetry assumptions as shown in Figs. 2a and 2b.

3.2. Material Model

In this study Johnson–Cook (J-C) material model [46] has been used, which provides a description of the plastic flow stress for the von mises criterion taking into account strain hardening, strain rate hardening and thermal softening as represented in Eq. 1.

$$\bar{\sigma}_{eq} = \left(A + B\bar{\varepsilon}_p^n\right)\ \left(1 + C\ln\left(\frac{\dot{\bar{\varepsilon}}_p}{\dot{\varepsilon}_0}\right)\right)\left(1 - \left(\frac{T - T_0}{T_m - T_0}\right)^m\right),\tag{1}$$

where $\bar{\varepsilon}_p$ is the equivalent plastic strain, $\dot{\bar{\varepsilon}}_p, \dot{\varepsilon}_0$ are the plastic and the reference strain rate accordingly. A is the initial yield strength of the material at quasi-static strain rate, B and n are the strain hardening modulus and exponent accordingly, C is the strain rate sensitivity parameter, m is the thermal softening coefficient. T_0 and T_m are the room and melting temperature respectively.

3.3. Equation of state

In laser shock simulation it is necessary to provide a thermodynamic relation to relate the sudden pressure, internal energy and density changes during the shock wave [47]. This was provided by the use of the equation of state described in this Section. Following the previous work of Ayad et al. [40], Johnson–Cook material model coupled with Grüneisen equation of state reproduce very well Al behavior under laser shock loading. We use Grüneisen equation of state as defined in LS-DYNA (EOS_GRUNEISEN) with cubic shock-velocity as a function of particle velocity $v_s(v_p)$. This defines different pressures for compressed and extended materials as the following Eqs. (2a) and (2b) accordingly.

$$p = \frac{\rho_0 C_0^2 \beta[1 + (1 - \frac{\gamma_0}{2})\beta - \frac{a}{2}\beta^2]}{[1 - (S_1 - 1)\beta - S_2\frac{\beta^2}{\beta+1} - S_3\frac{\beta^3}{(\beta+1)^2}]^2} + (\gamma_0 + a\beta)E\tag{2a}$$

$$p = \rho_0 C_0^2 \beta + (\gamma_0 + a\beta)E.\tag{2b}$$

Here C_0 is the intercept of $v_s(v_p)$ curve; S_1, S_2 and S_3 are the unitless coefficients of the slope of the $v_s(v_p)$ curve; γ_0 is the unitless Grüneisen gamma, a is the unitless first order volume correction to γ_0 and $\beta = \frac{\rho}{\rho_0} - 1$, E denotes the internal energy.

3.4. Pressure loading modeling

In this study, 3 mm focal spot has been used, whereas the FWHM of the spatial profile has been verified experimentally using a Charge-Coupled Device (CCD) camera. We used the smoothed spatial profile for the spatial distribution of the pressure produced by the laser plasma (Fig. 3a) which has been obtained and vali-
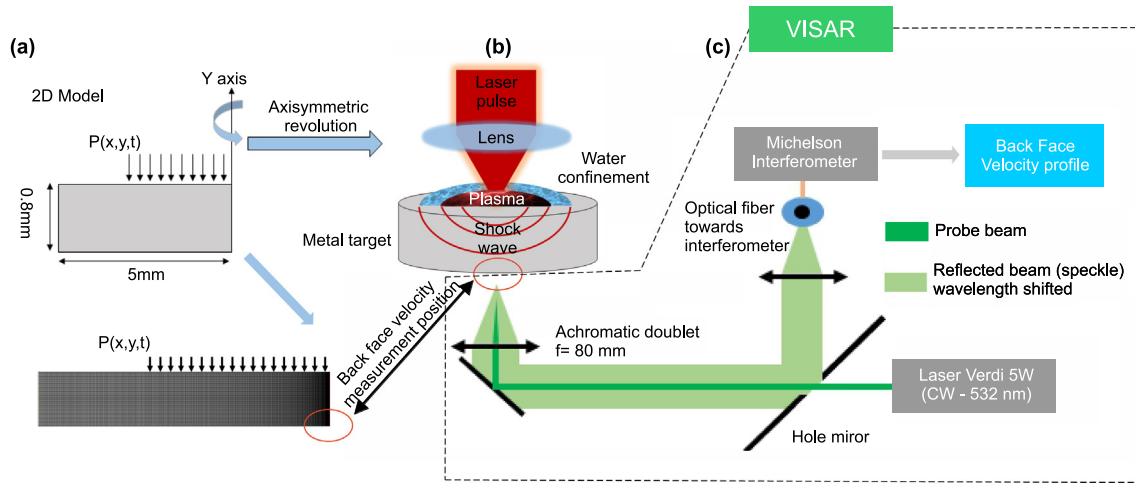
Fig. 2. (a) 2D Axisymmetric model used for shock wave simulation produced by the created plasma in a water confined regime (b) and coupled with the VISAR experimental measurement system (c).
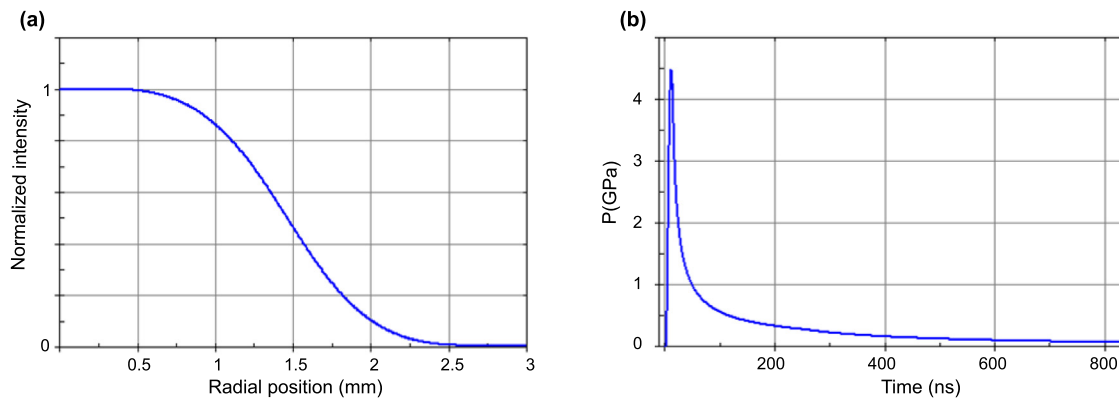
Fig. 3. (a) Spatial and (b) temporal pressure profile for 3 mm focal spot and 3.5 GW/cm^2 laser intensity.

dated with experimental measurements as has been used in previous work [40]. For the temporal pressure loading, the combined approach presented by Scius-Bertrand [48] and Rondepierre [49] as has been discussed in Ayad et al. [40] has been used (Fig. 3b).

4. Results

4.1. Microstrustuctural observations

Microstructures of BMs AA7075-T6 and AA2017-T4 in the S-T direction are shown in Figs. 4a and 4b, as EBSD inverse pole figure (IPF) maps along with the grain size distribution, respectively. Depicted results anticipated elongated grains in the S-T direction due to the rolling process, especially in the case of AA7075-T6. Quantitative grain size analysis confirms average grain size of ~35 ± 17µm (Fig. 4a), which is about 77% smaller compared to the AA2017-T4, consisting of more isotropic grains with the average size of ~62 ± 26µm (Fig. 4b).

In contrast, microstructure of the BMs in the L-T direction parallel to the rolling direction in Figs. 4c and 4d depict smaller effect of elongation with larger grains for AA2017-T4, where grains are randomly oriented and in the range of ~ 81 ± 36µm (Fig. 4d). Nonetheless, IPF of AA7075-T6 shows pronounced orientation in L direction, with the average grain size of ~156 ± 62 µm (Fig. 4c), being more than 300% larger compared to the grains in the S-T direction. In addition, the inset SEM/SE images in Fig. 4

depict that the number of intermetallic precipitates in AA2017-T4 is significantly higher compared to the AA7075-T6 alloy. The cross-section microstructures (S-T plane) of dissimilar FSW joint with the representative IPFs and grain size distribution are shown in Fig. 5. As depicted from microstructural observation, FSW region of 20 mm× 10 mm consists of five specific regions, i.e. heat affected zone (HAZ) on advancing side (AS), thermo-mechanically affected zone (TMAZ) on AS, nugget zone (NZ), TMAZ on retreating side (RS) and HAZ on RS. The unaffected BMs (Fig. 4) are farther on the left and right of the RS HAZ and AS HAZ, respectively. As depicted in macrograph in Fig. 5a, the NZ on the AS consists of a distinct banded structure, which gradually completely disappear toward RS, whereas microhardness values indicate different values of the specific region with an average microhardness of 155 HV$_{0.3}$ in the NZ. Further, the NZ/TMAZ boundary on RS is almost absent due to more gradual microstructure change and smaller grains in the TMAZ on RS, being in the range ~22 ± 14µm (Fig. 5b). On the contrary, the NZ/TMAZ boundary on the opposite AS is well-defined due to the rapidly microstructure variation and much larger grains of ~52 ± 20 µm, in the AS TMAZ region (Fig. 5d). Although, TMAZ microstructure on the specific side differentiates in morphology and grain size both indicate highly deformed microstructure and the traces of plastic flow in which the material flows around the rotating tool pin, but due to the insufficient energy and deformation strain, dynamic recrystallization (DRX) did not occur [22,50]. NZ, on the contrary consists of completely recrystallized, equiaxed grains but with some extend of texture
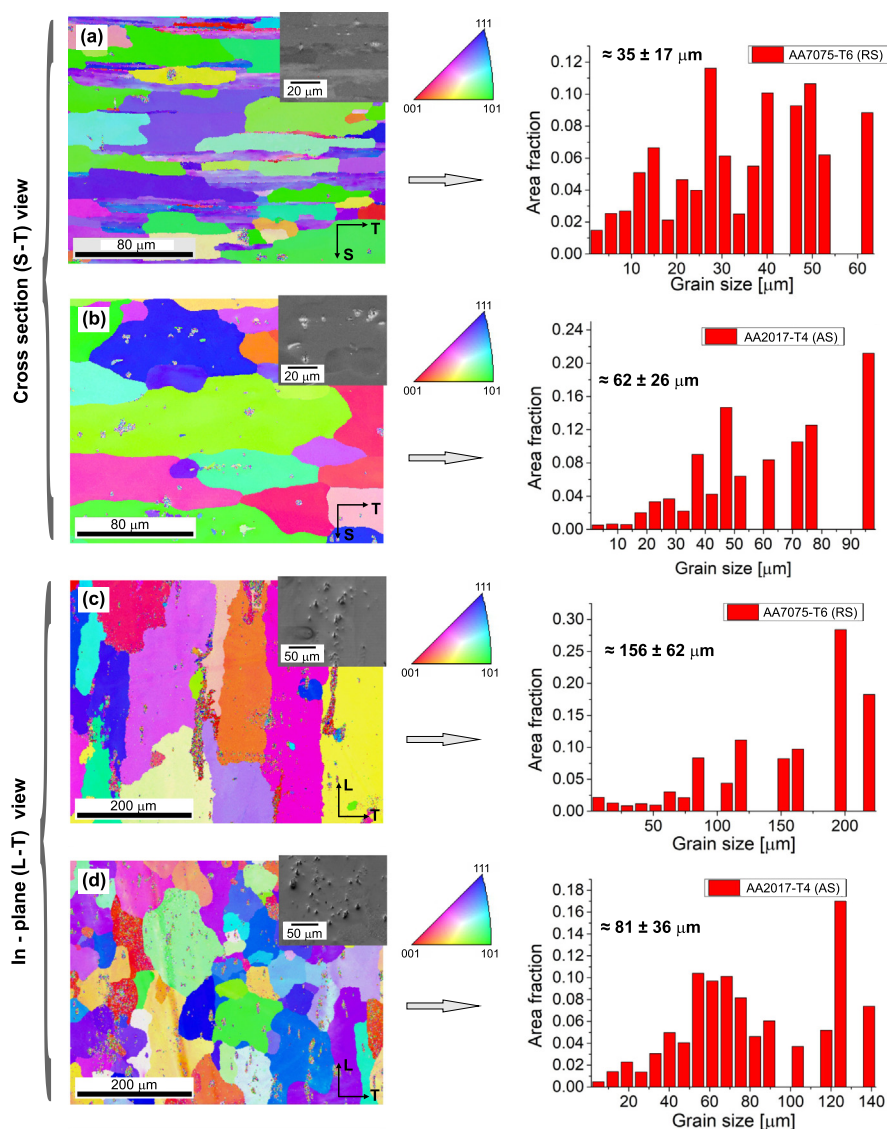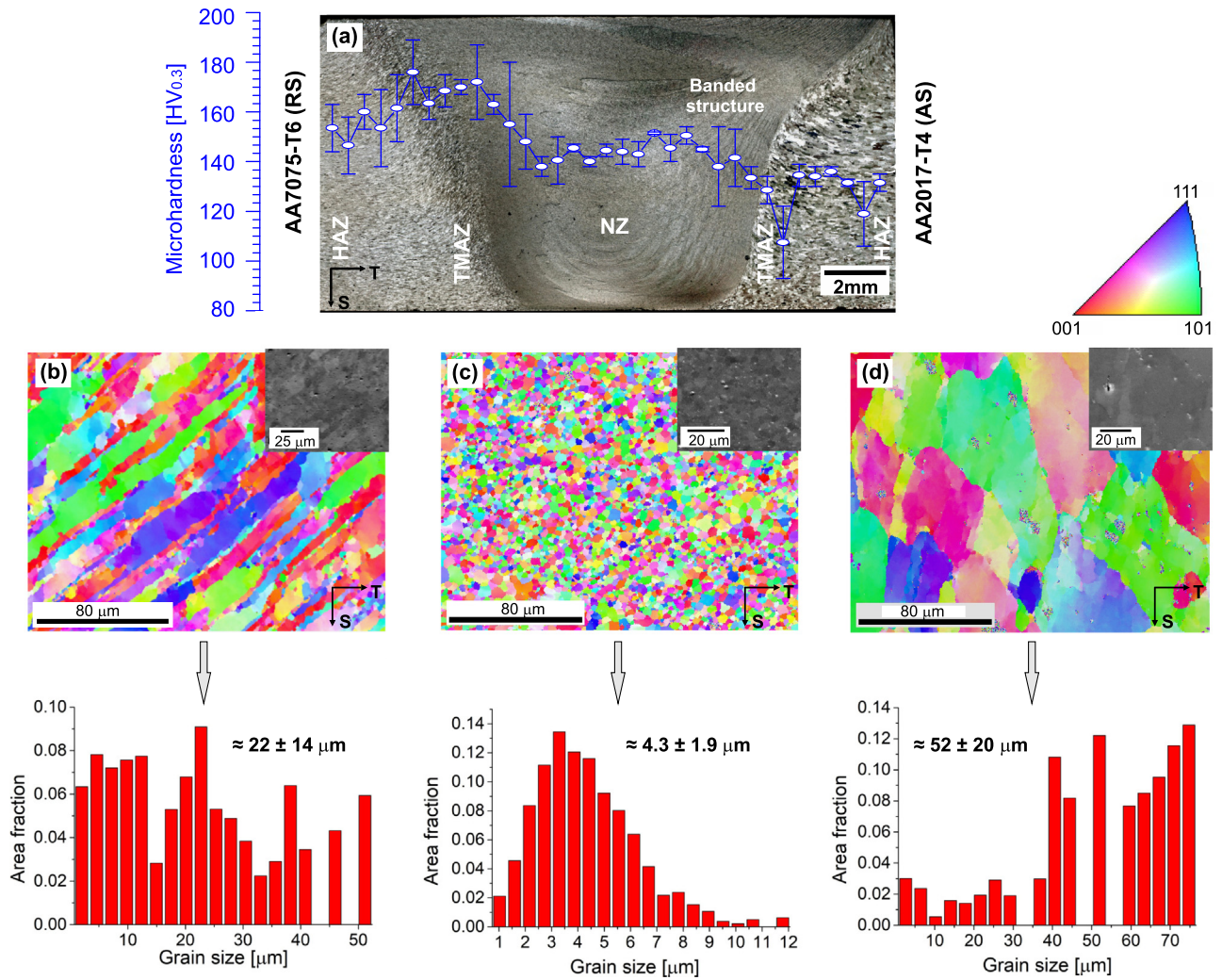
Fig. 4. EBSD IPF maps and grain size distribution of the BMs in the S-T (a,b) and L-T (c,d) planes for AA7075-T6 in (a,c) and for AA2017-T4 in (b,c) accordingly. (Insets: SEM/SEI showing intermetallic phases).

bands on AS side, consisting of smaller and larger DRX grains. Recently, Chen et al. [50] observed similar microstructural features in the cross-section of the FSWed ZK60 Mg alloy where in-depth microstructural characterization was conducted from the point of fatigue response and decisive roles on crack initiation behavior of the specific region. The same authors argued that the banded structure on the RS occurred during the FSW process since the material on the RS is trapped between the layers of the material on the AS which is primarily stirred in the interface region and thus forming a mixture. Similarly to our results banded structure consisted of lighter and darker bands, consisting of larger and smaller DRX crystal grains, due to different strain gradient as a consequence of asymmetric FSW plastic flow has been reported elsewhere [50–52]. Nonetheless, in the NZ, where further LSP shock wave propagation will be monitored, an average grain size, based on a larger area EBSD IPF analyses is ∼4.3 ± 1.9µm. The most representative image is shown in Fig. 5c.

The microstructural features of dissimilar 7075–2017 FSW joint in the in-plane (L-T) direction, below the crown of the weld are shown is Fig. 6. Macrograph in Fig. 6a, showing the different zones of the weld, with the microhardness profile along the joint, indi-

cates similar features as in the S-T direction, i.e. banded structure in the NZ and distinct NZ/TMAZ interface on the AS. However, by comparing the TMAZ regions in the L-T (Figs. 6b and d) with the S-T plane (Figs. 5b and d) a distinctive difference is observed. Further, microhardness results in the L-T plane indicate lower values compared to the S-T plane (137 vs. 155 $HV_{0.3}$) as shown in Figs. 6b, d and Figs. 5b, d respectively. If the latter showed clear "semi-circular" microstructural orientation due to FSW tool rotation, TMAZ regions in the L-T direction consists of highly deformed, elongated grains along the welding direction. In addition, in L-T larger grains are obtained, being in the range ∼61 ± 36µm on the retreating AA7075 side (Figs. 5b, and ∼85 ± 41µm on the advancing, AA2017 side (Fig. 6d). In addition, NZ in the L-T direction consists of ∼51% larger grains compared to the S-T plane, whereas a volume fraction of precipitates is larger in the L-T plane as well, for all the zones. Nonetheless, DRX grains in the NZ L-T plane are still very small and more or less equiaxed. Based on larger area examination and several EBSD IPF analyses an average grain size of ∼6.5 ± 2.6mm was determined (Fig. 6c).

The above mentioned differences are an outcome of several factors; (i) the origin itself, i.e. BMs which differ in the specific planes,

M. Ayad, L. Lapostolle, A. Rondepierre et al.

Fig. 5. (a) DM image of complete FSW CS (S-T) lamella with the microhardness ($HV_{0.3}$) profile along the middle region of the weld, (b-d) representative EBSD IPF maps and grain size distribution; (b) TMAZ on RS, (c) NZ and (d) TMAZ on AS. (Insets: SEM/SEI showing intermetallic phases).

having larger grains and larger amount of intermetallic phases in the L-T plane (see Figs. 4c and 4d) and (ii) different amount of simultaneous heat distribution and intense plastic deformation in the specific FSW joint plane and depth. The latter does not only affect the DRX grain size growth within the NZ, but also precipitates dissolution, secondary precipitation and re-distribution of intermetallic phases, which is more pronounced with higher temperature [22]. In the current literature, there are numerous investigations [22,18,50] focusing on temperature distribution and its effect on microstructural evolution, but mainly in the cross-section, i.e. S-T plane of the FSW joint. Nonetheless, the analogy regarding the heat input affecting grain growth and dissolution and coarsening of the second phase precipitates can be applied for the in-plane, i.e. L-T direction as well. Mishra et al. [22] reviewed a number of scientific papers concerning the temperature distribution during the FSW. Authors therein confirmed the peak temperature adjacent to the NZ on the top, crown side of the weld, which decreased to the bottom, i.e. root side of the weld. Such findings are rather expected, taking into account the effect of the shoulder-workpiece interface during FSW on the heat input generation [53]. Nonetheless, despite the fact that the tool shoulder predominantly affects the heat input, tool pin also has also role on the temperature distribution within the weld. Considering flat, i.e. non-concave tool shoulder the total head generated by the FSW is [54]:

$$Q = \frac{2}{3} \mu \omega F [R_s + 3 \frac{R_p^2 H_p}{R_s^2}] \qquad (3)$$

where, Q[kW] is the heat input during FSW, μ is the friction of coefficient, ω[rad/s] is the angular velocity, F[kN] is axial force, H_p[m] represents the height of tool pin and R_s and R_p[m] is the radius of tool shoulder and pin, respectively.
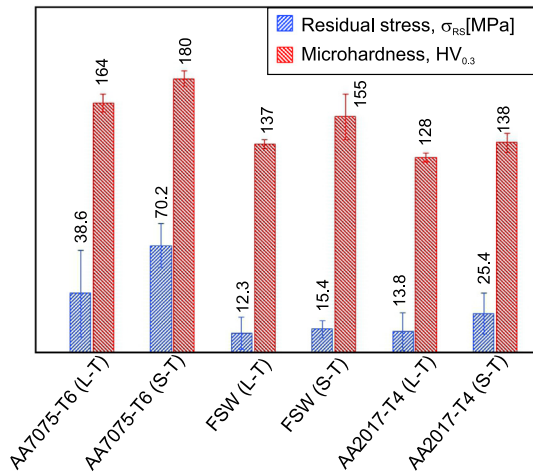
4.2. Residual stress and microhardness

It is well known that specific regions and planes of the FSW joint indicate profound variations in residual stresses and microhardness, contributing to different behavior under cyclic loading, corrosion, creep, and other mechanical loadings. Hence, in order to investigate mechanical properties of the specific lamellas which will be further investigated by LSP shock wave loading and BFV analyses, measurements of RS and microhardness measurements were conducted and compare it among each other. As results in Fig. 7 depicts the specific plane (S-T vs. L-T) has a significant influence microhardness and RS value. Furthermore, a perfect correlation between RS and microhardness is observed, being almost linearly dependent. Microhardness of AA7075-T6 measured along the S-T plane is ~25% higher than in the L-T plane (180 ± 5 $HV_{0.3}$ vs. 164 ± 6 $HV_{0.3}$) and almost 82% higher tensile RS (70.2
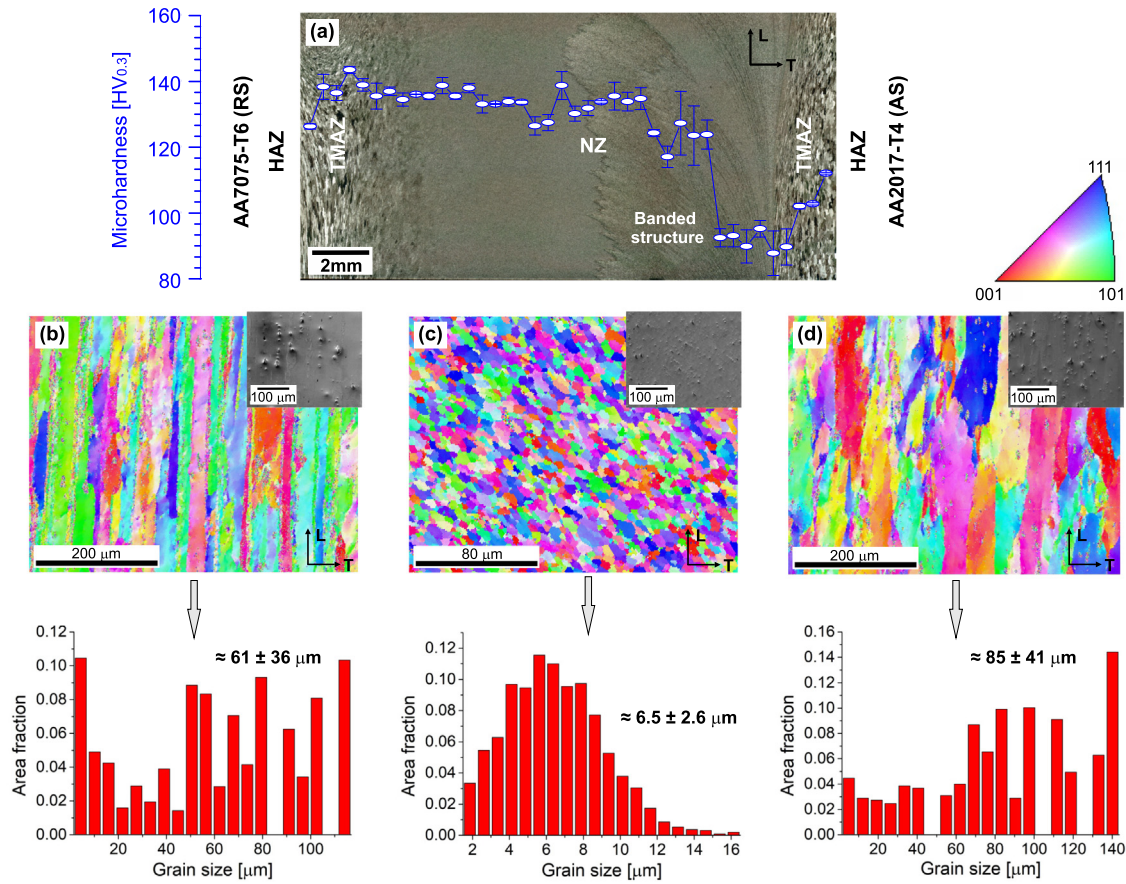
Fig. 6. (a) DM image of complete FSW IP(L-T) lamella with the microhardness (HV$_{0.3}$) profile along the middle region of the weld, (b-d) representative EBSD IPF maps and grain size distribution; (b) TMAZ on RS, (c) NZ and (d) TMAZ on AS. (Insets: SEM/SEI showing intermetallic phases).

Fig. 7. Comparison between residual stresses (RS) and microhardnes HV$_{0.3}$ for specific regions and planes of AA7075-T6, AA2017-T4 and the dissimilar FSW 7075–2017 joint.

± 14.5 MPa vs. 38.6 ± 28.5 MPa). Similar results are also observed for AA2017-T4 with an average microhardness and RS of 138 ± 6 HV$_{0.3}$ & 25.4 ± 13.4 MPa, and 128 ± 3 HV$_{0.3}$ & 13.8 ± 12.4 MPa for the S-T an L-T plane, respectively.

Although, microhardness values in the NZ of FSW showed some scattering (especially in the S-T plane), mainly due to the banded/-textured structure, having also the chemical composition of both Al alloys, the hardness is higher compared to the AA2017-T4, for both

measured planes. Analyses showed average microhardness of 155 ± 15 HV$_{0.3}$ (S-T) and 137 ± 3 HV$_{0.3}$ (L-T), respectively. These results are consistent with the microstructural observations in the previous subsection, indicating that larger heat-input in the L-T plane leads to more extensive grain growth during DRX, dissolution and coarsening of strengthening precipitates, which contribute to inferior mechanical properties, which is also confirmed by the microhardness results across the weld region (Figs. 5 and 6). Similarly, a higher tensile RS was also obtained for the S-T plane (15.4 ± 5.6 MPa vs. 12.3 ± 10.4 MPa). Such results indicate close to zero RS state, which is in accordance with RS results on AA2017-T451 BM sample and with our previously published results [13].

4.3. Influence of material properties on the dynamical high strain rate behavior

Numerical investigation of the material model was based on experimental BFV measurement of Al alloys under laser shock loading. Therefore, we studied the influence of material model parameters on the BFV, in order to know which material model parameter should be adjusted until we reproduce the experimental behavior. To that scope, we used Pure Al case study since material model has been already validated in previous work [55]. We obtained the BFV curve associated with the axial stress propagation through 1 mm thickness of Pure Al under 0.8 GW/cm² laser intensity and 3 mm focal spot (Fig. 8), using validated material model parameters [55,56] as has been used in previous work [40].

Fig. 8 depict signature of axial stress propagation σ_{yy} during the laser shock through the target thickness. More importantly, the blue arrows present the compression shock which propagates at
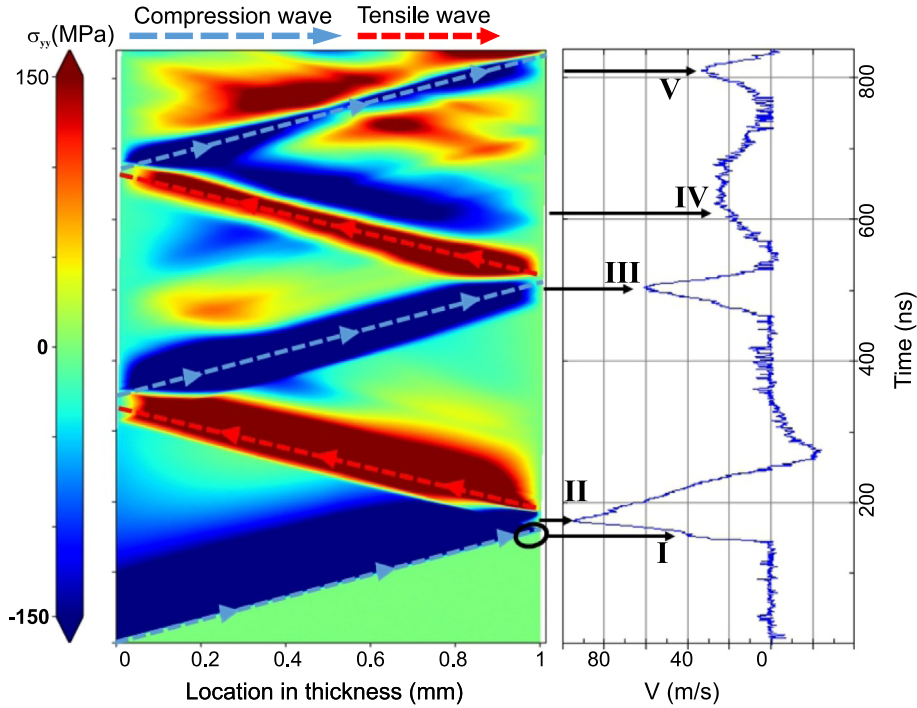
Fig. 8. Axial compression and tension stress level σ_{yy} (blue and red arrows respectively) during the wave propagation through the Pure Al sample (horizontal axis) and during the laser shock loading under 0.8 GW/cm² with the associated BFV profile.

two different velocities (faster elastic and slower plastic waves) where the transition between them can be seen by the elastic precursor which can be detected on the front of the BFV curve (point I). The plastic wave continues to propagate towards the back face and produce the first peak as we see in the BFV profile (point II). The signatures of the propagating shock waves and the associated 2D phenomena are marked on the BFV profile by Roman numbers and described in Table 3.

The influence of material model parameters on the BFV profile has been analyzed on Pure Al as shown in Fig. 9 using 3 mm focal spot and 0.8 GW/cm² laser intensity since it shows all 2D signature on BFV of 1 mm Pure Al target as ($P_{max}/P_{HEL} < 13$) according to Table 3. In regards of the intercept of $v_s(v_p)$ in the equation of state, C_0 can be adjusted until the first shock breaks out at the same time of the experimental shock. Other two parameters of the equation of state (S_1 and γ_0) have negligible influence on the BFV profile, so their values will be 1.338 and 2 as the Pure Al parameters.

Fig. 9 reveals the influence of material properties on the BFV profiles. It can be noticed that material density and shear modulus variation (Figs. 9a and 9b) has a negligible effect on the maximum velocity (point II in Fig. 8), however we can notice some difference
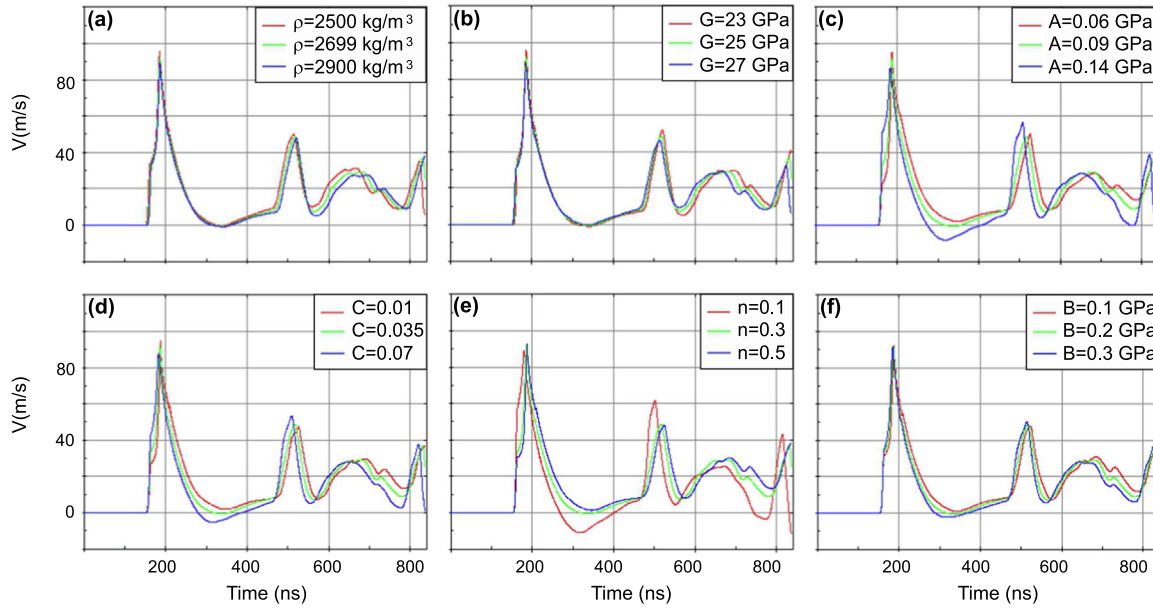
on the front of second peak (point III in Fig. 8) and on the signature of 2D phenomena (point IV in Fig. 8). Concerning J-C parameters influence on the BFV profile, elastic precursor is hypersensitive on the initial yield strength A and strain rate hardening coefficient C as shown in Figs. 9c and d, while the strain hardening parameter n changes the slope of the plastic waves upon the elastic precursor as shows Fig. 9e. The strain hardening parameter B has the same influence as n with lower less magnitude on the entire BFV profile (Fig. 9f). The parameter C_0 and the ones whose influences are discussed in Fig. 9 are the key materials properties required for the simulation.

4.4. Validation of the optimized material model

Experiments were performed using 3 mm focal spot and under 3.5 GW/cm² laser intensity applied on two different thicknesses of each material (approximately 0.8 and 1.2 mm ± 5 % of tolerance). After experimental measurement of material response under laser shocks, simulation has been performed and material model parameters have been optimized until the simulation reproduce the experimental results. For each material, we are going to present the obtained mechanical and J-C parameters based on the corresponding BFV profile which reproduces the experimental behavior under laser shock.

We have started with the AA7075-T6, distinguishing between L-T and S-T configurations as the difference lies in the dynamic behavior under laser shock. We optimized literature parameters (Tables 1,2) for each configuration until the numerical model reproduces the experimental behavior as shown in Fig. 10. To that scope, we followed the influence of each parameter on the dynamical response as illustrated in Fig. 9.

The optimized numerical parameters in Table 4 reproduce the experimental results for each configuration (L-T) and (S-T) in Figs. 10 (a,c) and (b,d) for two thicknesses 0.8 and 1.2 mm accordingly. The optimized material model parameters used in Fig. 10 are listed in Table 4.

Table 3

Origin of Pure Al BFV peaks according to the signature of axial stress propagation induced by laser shock on the back face of Pure Al of 1 mm thickness under 0.8 GW/cm² and 3 mm focal spot.

Notations	Definition
I	Shoulder separating the fast elastic wave from the slower plastic wave[57,58]
II	1st shock breaking out
III	2nd shock breaking out which corresponds to the back and forth of the first one
IV	2D shock breaking out which vanishes when: $P_{max}/P_{HEL} \geq 13$ [40]
V	3rd shock breaking out which corresponds to the back and forth of the second one

Fig. 9. Influence of the specific material model parameters on the BFV of 1 mm Pure Al plate using 3 mm focal spot under 0.8 GW/cm² laser intensity; (a) density ρ, (b) shear modulus G, (c) initial yield strength A, (d) strain rate sensitivity C, (e) strain hardening exponent n, (f) strain hardening modulus B.
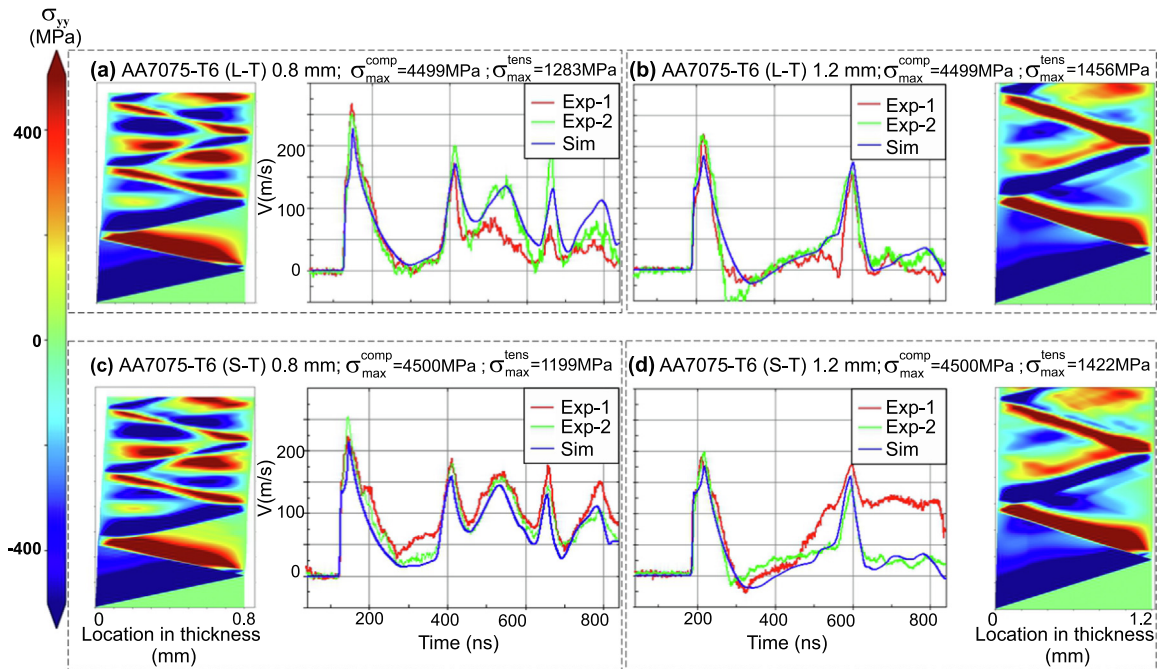
Fig. 10. Experimental (Exp-1 and Exp-2) and simulation (Sim) velocity profiles for two different thicknesses and planes of AA7075-T6 under 3.5 GW/cm² laser intensity; (a,b) L-T with 0.8 and 1.2 mm; (c,d) S-T with 0.8 and 1.2 mm.

Table 4
Johnson–Cook parameters and mechanical properties of AA7075-T6 (L-T) and (S-T) configurations.

Material	ρ(kg/m³)	G(GPa)	C_0(m/s)	A(MPa)	B(MPa)	C	n
AA7075-T6 (L-T)	2800	30	5000	400	800	0.05	0.45
AA7075-T6 (S-T)	2820	31	5150	473	210	0.033	0.3813

The same methodology has been applied for AA2017-T4, where the literature parameters from Tables 1,2 have been optimized until the numerical solution reproduce the experimental measurements of the BFV for each configuration of AA2017-T4 as shown in Fig. 11. The optimized material model parameters used in Fig. 11 are listed in Table 5.

After we proved that we are able to obtain a proper material model for both AA2017-T4 and AA7075-T6 we performed numer-

ous simulations of the FSW (L-T) and (I-P) behavior. Different parameters have been used, starting with the one obtained in Tables 5 and 4 until we obtained the closer behavior to the experimental one as shown in Fig. 12. The optimized material model parameters used in Fig. 12 are listed in Table 6.

As depicted in Fig. 12, the optimized numerical material parameters provided a good correlation between simulation and experimental measurements of the BFV profile.

5. Discussion

The combined experimental investigations of microstructural and mechanical properties, BFV and numerical study presented here provide new insights of material behavior under laser shock loading. It is worth noting that material behavior at high strain rate of AA2050-T8, AA2050-T3 and FSW AA2050-T3 joint has already been reported [39]. However, therein the material model validation by experimental and numerical analyses covered only the first period of laser shock propagation through the material. Furthermore, the investigation considered just one, i.e. cross section material plane, whereas the effect of the material anisotropy regarding microstructural and mechanical properties was not taken into account. However, this is very important and requires consideration since the microstructure of wrought Al alloys is quite complex, with different crystal grain size and orientations in the specific plane due to the preliminary rolling. Moreover, different amount of rolling reductions in the specific layer [17,59] results in Al matrix with a wide range of intermetallic phases [11,12]. Hence, material response and properties to dynamic loading can differ accordingly in the specific plane. In the FSW joint, it can be even more complex especially in the case when two different alloys are involved each having its chemical composition and intermetallic phases. In this work, the difference between sections or planes has been investigated on Al samples before and during laser shock loading. Mechanical features (i.e. residual stresses and microhardness variations) features have been analyzed (see Fig. 7), and relative difference of material model parameters between S-T and L-T configurations have been obtained (see Fig. 13).

Obtained results in the form of relative difference display significant effect of the material plane, especially for the J-C parameters B, C and n. Thus, the relative difference of strain hardening parameter B was found to be in the following order: 73.8% (AA7075-T6) < 60 % (FSW) < 50 % (AA2017-T4). In contrast, the highest relative difference of strain-rate sensitivity parameter C and strain hardening exponent n has been found for FSW (48.9 %) and for AA2017-T4 (50 %), respectively.

In order to examine microstructural effect on the material dynamic response under high-strain rate loading, J-C model parameters are depicted separately in Fig. 14 along with the grain size and residual stress (RS) values, for the investigated regions and planes of the FSWed joint.

From the given results, it is clear that the grain size and mechanical state, i.e. RS and HV, which are in perfect correlation (see Fig. 7), has a direct influence on the J-C material parameters. As discussed in the previous sections, smaller grain size (Section 4.1), higher tensile RS, as well as higher microhardness values (Section 4.2) are obtained in the cross-section (S-T) direction, within all the investigated regions of the FSW joint. Such initial material state contribute to higher yield strength A, shear modulus G and density ρ (Figs. 14a, e and f), although the difference in the density is negligible. Those material features are associated with higher strain, dislocation density and it is in accordance with the Hall–Petch effect [39]. On the contrary, J-C strain dependent parameters B, C and n decrease with smaller grain size and higher RS (Figs. 14b-d), due to poorer material ductility. This effect is remarkably evident in the case of AA7075-T6 region in which material plane and its condition remarkably affect the strain hardening modulus B (see Fig. 14b). Here the highest anisotropy with biggest difference in grain size, RS and HV values was confirmed among S-T and L-T planes. The change in strain hardening modulus B is relatively smaller for AA2017-T4 and accordingly smallest for FSW NZ region where grain size and RS of the specific plane differ the least.

Similar behavior was noticed also for the strain-rate sensitivity parameter C (see Fig. 14b) and work hardening exponent n (see Fig. 14d). These findings are in good accordance with other studies [60] indicating that the reduction of grain size contributes to the increase of the J-C von Mises flow stress.
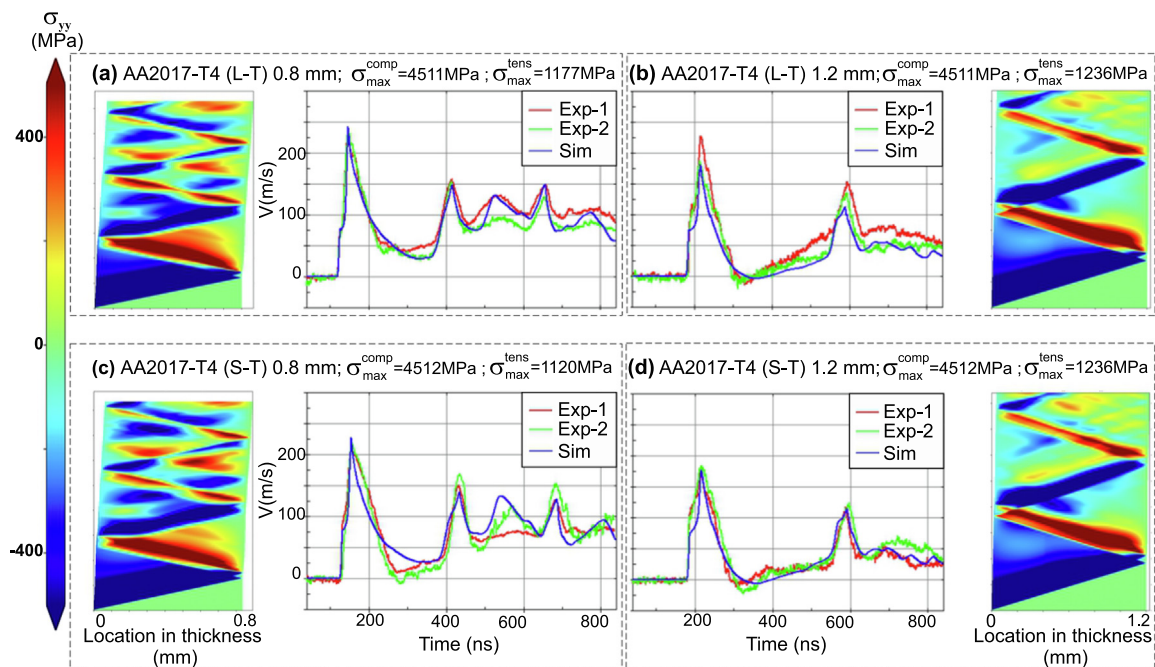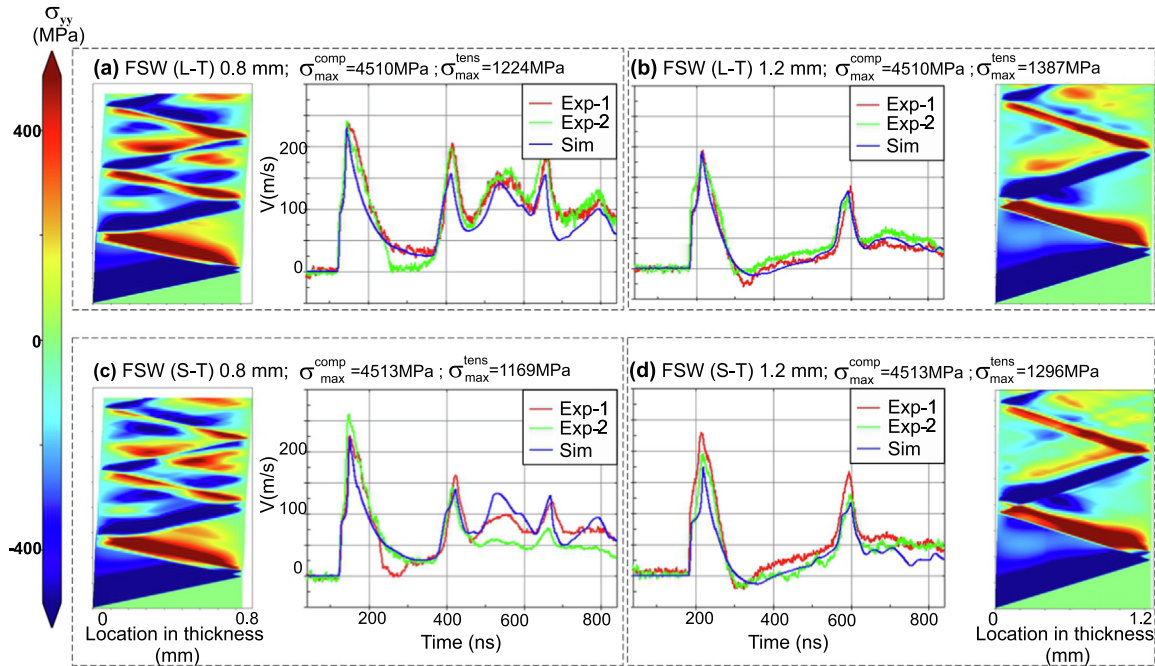

Fig. 11. Experimental (Exp-1 and Exp-2) and simulation (Sim) velocity profiles for two different thicknesses and planes of AA2017-T4 under 3.5 GW/cm² laser intensity; (a,b) L-T with 0.8 and 1.2 mm; (c,d) S-T with 0.8 and 1.2 mm.

Table 5
Johnson–Cook parameters and mechanical properties of AA2017-T4 (L-T) and (I-P) configurations.

Material	$\rho(\text{kg/m}^3)$	$G(\text{GPa})$	$C_0(\text{m/s})$	$A(\text{MPa})$	$B(\text{MPa})$	C	n
AA2017-T4 (L-T)	2780	31	5380	260	700	0.035	0.6
AA2017-T4 (S-T)	2800	32	5300	270	350	0.03	0.3

Fig. 12. Experimental (Exp-1 and Exp-2) and simulation (Sim) velocity profiles for two different thicknesses and planes of FSW 2017–7075 under 3.5 GW/cm² laser intensity; (a,b) L-T with 0.8 and 1.2 mm; (c,d) S-T with 0.8 and 1.2 mm.

Table 6
Johnshon Cook parameters and mechanical properties of FSW (L-T) and (I-P) configurations.

Material	$\rho(\text{kg/m}^3)$	$G(\text{GPa})$	$C_0(\text{m/s})$	$A(\text{MPa})$	$B(\text{MPa})$	C	n
FSW (L-T)	2790	28	5350	285	500	0.033	0.35
FSW (S-T)	2810	33	5500	340	200	0.017	0.2

**Fig. 13.** Relative difference of material parameters between S-T and L-T configurations.

6. Conclusion and outlook

A novel methodology is proposed to asses dynamical behavior under laser shock loading of Al alloys and dissimilar FSWed joint, manufacured using optimised parameters. In order to obtain in-depth information of material behaviour in a high strain rate regime dynamic experiments, microstructural features and numerical simulations has been performed. At the same time material anisotropy, which differs according to the specific material plane, due to preliminary rolling and welding direction has been taken into account. Based on the obtained new insights, the following conclusions can be depicted:(*i*) The proposed methodology has confirmed direct relationship between dynamical behavior in a nano-second time scale and microstructural features which can serve for a fast assesment of material properties even for dissimilar pairs and different material planes.(*ii*) Detailed analyses revealed that strain hardening and strain rate sensitivity parameters *B* and *C* are directly affected by the microstructural properties, whereas the texture predominately affects strain rate modulus *B*, having the highest variation between S-T and L-T material planes. Hence, the biggest difference of the strain rate modulus *B* has been confirmed for AA7075-T6, whilst the biggest difference of strain rate sensitivity parameter *C* and strain hardening exponent *n* has been confirmed with the FSW joint and AA2017-T4, respectively.(*iii*) Results have confirmed a perfect correlation between residual stresses and microhardness. For example, microhardness and RS of AA7075-T6 along S-T plane are higher for 10 % and 82 % than in the L-T plane, respectively.

Findings obtained in the scope of this research contribute to comprehensive understanding of material behavior under high
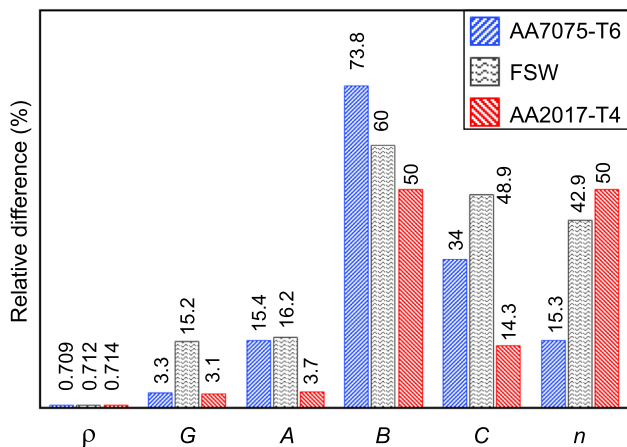
M. Ayad, L. Lapostolle, A. Rondepierre et al.
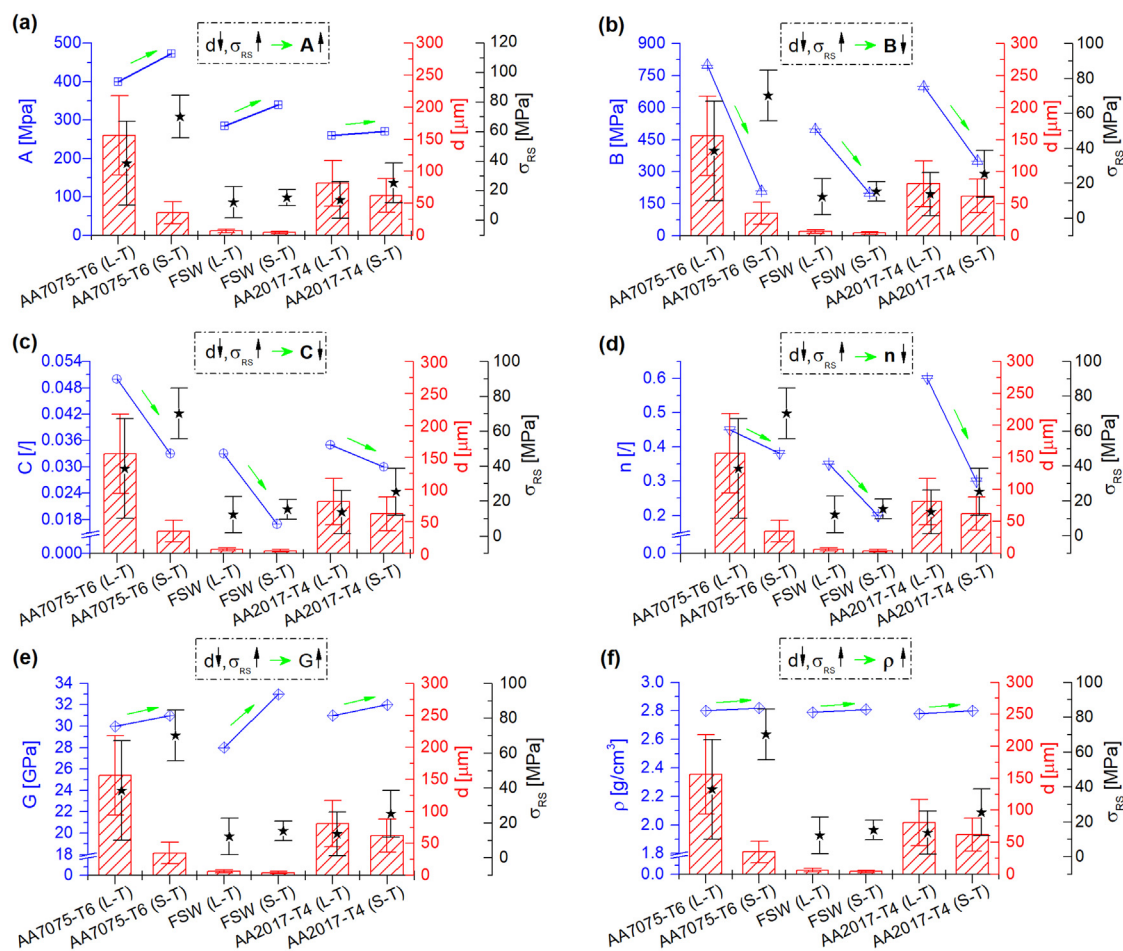
Fig. 14. Correlation between grain size, residual stress and material model parameters in specific regions and planes of dissimilar FSW 7075–2017 joint; (a) initial yield strength *A*, (b) strain hardening modulus *B*, (c) strain rate sensitivity *C*, (d) strain hardening exponent *n*, (e) shear modulus *G* and (f) density *ρ*.

strain rates triggered by laser shock impacts. Considering the obtained results it is noteworthy that, the specific observation holds true by comparing initial material properties and J-C parameters between the planes of specific regions/materials but not all the regions among themselves. This is rather expected since each region of dissimilar FSWed joint has different grain size morpohology and chemical composition. Furthermore, in the FSW joint additional heat-treatment occurred, i.e. DRX and precipitation dissolution and re-precipitation. This effect has completely eliminated all the traces/birth-marks of prior technological production phases such as rolling, solution treatment and ageing which was present with the BMs. Hence, the anisotropy was highlighted by introducing two different sets of parameters, i.e. material planes (L-T & S-T) because the material model was isotropic. However, with the current methodology, investigating the anisotropy feature in different directions could be time and cost consuming. Nonetheless, the developed methodology can be used for both, i.e. raw and welded metallic alloys in manufacturing science community and can also serve as the potential candidate in industrial applications for optimization of laser shock penning process.

7. Data availability statement

The data that support the findings of this study are available from the corresponding author upon reasonable request.

Declaration of Competing Interest

The authors declare that they have no known competing financial interests or personal relationships that could have appeared to influence the work reported in this paper.

References

[1] S. Ünaldi, K. Papadopoulos, A. Rondepierre, Y. Rouchausse, A. Karanika, F. Deliane, K. Tserpes, G. Floros, E. Richaud, L. Berthe, Towards selective laser paint stripping using shock waves produced by laser-plasma interaction for aeronautical applications on aa 2024 based substrates, Opt. Laser Technol. 141 (2021) 107095, https://doi.org/10.1016/j.optlastec.2021.107095.

[2] L. Zhu, N. Li, P. Childs, Light-weighting in aerospace component and system design, Propul. Power Res. 7 (2) (2018) 103–119, https://doi.org/10.1016/j.jppr.2018.04.001.

[3] M. Besel, Y. Besel, U. Alfaro Mercado, T. Kakiuchi, Y. Uematsu, Fatigue behavior of friction stir welded al–mg–sc alloy, Int. J. Fatigue 77 (2015) 1–11, https://doi.org/10.1016/j.ijfatigue.2015.02.013.

[4] K. Martinsen, S. Hu, B. Carlson, Joining of dissimilar materials, CIRP Ann. 64 (2) (2015) 679–699, https://doi.org/10.1016/j.cirp.2015.05.006.

[5] T. Wang, S. Sinha, M. Komarasamy, S. Shukla, S. Williams, R.S. Mishra, Ultrasonic spot welding of dissimilar al 6022 and al 7075 alloys, J. Mater. Process. Technol. 278 (2020) 116460, https://doi.org/10.1016/j.jmatprotec.2019.116460.

[6] J. Oliveira, K. Ponder, E. Brizes, T. Abke, P. Edwards, A. Ramirez, Combining resistance spot welding and friction element welding for dissimilar joining of aluminum to high strength steels, J. Mater. Process. Technol. 273 (2019) 116192, https://doi.org/10.1016/j.jmatprotec.2019.04.018.

[7] J. Yang, J. Oliveira, Y. Li, C. Tan, C. Gao, Y. Zhao, Z. Yu, Laser techniques for dissimilar joining of aluminum alloys to steels: A critical review, J. Mater. Process. Technol. 301 (2022) 117443, https://doi.org/10.1016/j.jmatprotec.2021.117443.

[8] J. Oliveira, J. Duarte, P. Inácio, N. Schell, R. Miranda, T.G. Santos, Production of al/niti composites by friction stir welding assisted by electrical current, Materials & Design 113 (2017) 311–318, https://doi.org/10.1016/j.matdes.2016.10.038.

[9] S.H. Huang, P. Liu, A. Mokasdar, L. Hou, Additive manufacturing and its societal impact: a literature review, Int. J. Adv. Manuf. Technol. 67 (5–8) (2013) 1191–1203, https://doi.org/10.1007/s00170-012-4558-5.

[10] L. Pérez, S. Rodríguez-Jiménez, N. Rodríguez, R. Usamentiaga, D.F. García, L. Wang, Symbiotic human–robot collaborative approach for increased productivity and enhanced safety in the aerospace manufacturing industry, Int. J. Adv. Manuf. Technol. 106 (3–4) (2020) 851–863, https://doi.org/10.1007/s00170-019-04638-6.

[11] U. Trdan, T. Sano, D. Klobcar, Y. Sano, J. Grum, R. Šturm, Improvement of corrosion resistance of aa2024-t3 using femtosecond laser peening without protective and confining medium, Corros. Sci. 143 (2018) 46–55, https://doi.org/10.1016/j.corsci.2018.08.030.

[12] U. Trdan, J. Grum, SEM/EDS characterization of laser shock peening effect on localized corrosion of al alloy in a near natural chloride environment, Corros. Sci. 82 (2014) 328–338, https://doi.org/10.1016/j.corsci.2014.01.032.

[13] U. Trdan, M. Skarba, J.A. Porro, J.L. Ocaña, J. Grum, Application of massive laser shock processing for improvement of mechanical and tribological properties, Surf. Coat. Technol. 342 (2018) 1–11, https://doi.org/10.1016/j.surfcoat.2018.02.084.

[14] C. He, Y. Liu, J. Dong, Q. Wang, D. Wagner, C. Bathias, Fatigue crack initiation behaviors throughout friction stir welded joints in aa7075-t6 in ultrasonic fatigue, Int. J. Fatigue 81 (2015) 171–178, https://doi.org/10.1016/j.ijfatigue.2015.07.012.

[15] J.K. Sunde, D.N. Johnstone, S. Wenner, A.T. van Helvoort, P.A. Midgley, R. Holmestad, Crystallographic relationships of t-/s-phase aggregates in an al–cu–mg–ag alloy, Acta Mater. 166 (2019) 587–596, https://doi.org/10.1016/j.actamat.2018.12.036.

[16] Y. Zhu, K. Sun, G.S. Frankel, Intermetallic phases in aluminum alloys and their roles in localized corrosion, Journal of The Electrochemical Society 165 (11) (2018) C807–C820, https://doi.org/10.1149/2.0931811jes.

[17] U. Trdan, M. Skarba, J. Grum, Laser shock peening effect on the dislocation transitions and grain refinement of al–mg–si alloy, Mater. Charact. 97 (2014) 57–68, https://doi.org/10.1016/j.matchar.2014.08.020.

[18] P. Cavaliere, R. Nobile, F. Panella, A. Squillace, Mechanical and microstructural behaviour of 2024–7075 aluminium alloy sheets joined by friction stir welding, International Journal of Machine Tools and Manufacture 46 (6) (2006) 588–594. doi:10.1016/j.ijmachtools.2005.07.010.

[19] M. Koilraj, V. Sundareswaran, S. Vijayan, S. Koteswara Rao, Friction stir welding of dissimilar aluminum alloys aa2219 to aa5083 – optimization of process parameters using taguchi technique, Materials & Design 42 (2012) 1–7, https://doi.org/10.1016/j.matdes.2012.02.016.

[20] B. Gibson, D. Lammlein, T. Prater, W. Longhurst, C. Cox, M. Ballun, K. Dharmaraj, G. Cook, A. Strauss, Friction stir welding: Process, automation, and control, Journal of Manufacturing Processes 16 (1) (2014) 56–73, recent Developments in Welding Processes. doi:10.1016/j.jmapro.2013.04.002.

[21] W. Thomas, P. Threadgill, E. Nicholas, Feasibility of friction stir welding steel, Sci. Technol. Weld. Joining 4 (6) (1999) 365–372, https://doi.org/10.1179/136217199101538012.

[22] R. Mishra, Z. Ma, Friction stir welding and processing, Materials Science and Engineering: R: Reports 50 (1) (2005) 1–78, https://doi.org/10.1016/j.mser.2005.07.001.

[23] M. Simoncini, D. Ciccarelli, A. Forcellese, M. Pieralisi, Micro- And macro-mechanical properties of pinless friction stir welded joints in AA5754

aluminium thin sheets, Procedia CIRP 18 (2014) 9–14, https://doi.org/10.1016/j.procir.2014.06.099.

[24] A. Smolej, D. Klobcar, B. Skaza, A. Nagode, E. Slacek, V. Dragojevic, S. Smolej, Superplasticity of the rolled and friction stir processed al–4.5 mg–0.35sc–0.15zr alloy, Materials Science and Engineering: A 590 (2014) 239–245, https://doi.org/10.1016/j.msea.2013.10.027.

[25] R. Chandran, S. Ramaiyan, A.G. Shanbhag, S. Santhanam, Optimization of Welding Parameters for Friction Stir Lap Welding of AA6061-T6 Alloy, Modern Mechanical Engineering 08 (01) (2018) 31–41, https://doi.org/10.4236/mme.2018.81003.

[26] G. D'Urso, C. Giardini, The influence of process parameters and tool geometry on mechanical properties of friction stir welded aluminum lap joints, Int.J. Mater. Form. 3 (SUPPL. 1) (2010) 1011–1014, https://doi.org/10.1007/s12289-010-0941-7.

[27] S. Señorís-Puentes, R.F. Serrano, G. González-Doncel, J.H. Hattel, O.V. Mishin, Microstructure and mechanical properties of friction stir welded aa6061/aa6061 + 40% vol sic plates, Metals 11 (2) (2021) 1–11, https://doi.org/10.3390/met11020206.

[28] L. Fratini, B. Zuccarello, An analysis of through-thickness residual stresses in aluminium fsw butt joints, Int. J. Mach. Tools Manuf 46 (6) (2006) 611–619, https://doi.org/10.1016/j.ijmachtools.2005.07.013.

[29] M.M. Ahmed, M.I. Habba, N. Jouini, B. Alzahrani, M.M. El-Sayed Seleman, A. El-Nikhaily, Bobbin tool friction stir welding of aluminum using different tool pin geometries: Mathematical models for the heat generation, Metals 11 (3) (2021) 1–19. doi:10.3390/met11030438.

[30] M. Simoncini, A. Costa, S. Fichera, A. Forcellese, Experimental analysis and optimization to maximize ultimate tensile strength and ultimate elongation of friction stir welded aa6082 aluminum alloy, Metals 11 (1) (2021) 1–21, https://doi.org/10.3390/met11010069.

[31] C. Vimalraj, P. Kah, Experimental review on friction stir welding of aluminium alloys with nanoparticles, Metals 11 (3) (2021) 1–28, https://doi.org/10.3390/met11030390.

[32] A. Dimopoulos, A. Vairis, N. Vidakis, M. Petousis, On the friction stir welding of al 7075 thin sheets, Metals 11 (1) (2021) 1–12, https://doi.org/10.3390/met11010057.

[33] M. Grujicic, B. Pandurangan, C.F. Yen, B.A. Cheeseman, Modifications in the AA5083 Johnson-Cook material model for use in friction stir welding computational analyses, J. Mater. Eng. Perform. 21 (11) (2012) 2207–2217, https://doi.org/10.1007/s11665-011-0118-7.

[34] P. Liu, J. Hu, S. Sun, S. Xu, G. Ren, Effect of laser shock peening on the microstructural characterization in weld nugget zone of friction stir welded 7050 aluminum alloys, Journal of Laser Applications 30 (3) (2018) 032015, https://doi.org/10.2351/1.5035483.

[35] O. Hatamleh, J. Lyons, R. Forman, Laser and shot peening effects on fatigue crack growth in friction stir welded 7075–t7351 aluminum alloy joints, Int. J. Fatigue 29 (3) (2007) 421–434, https://doi.org/10.1016/j.ijfatigue.2006.05.007.

[36] A.H. Feng, D.L. Chen, Z.Y. Ma, Microstructure and low-cycle fatigue of a friction-stir-welded 6061 aluminum alloy, Metall. Mater. Trans. A 41 (10) (2010) 2626–2641, https://doi.org/10.1007/s11661-010-0279-2.

[37] T. Voisin, M. Grapes, T. Li, M. Santala, Y. Zhang, J. Ligda, N. Lorenzo, B. Schuster, G. Campbell, T. Weihs, In situ tem observations of high-strain-rate deformation and fracture in pure copper, Mater. Today 33 (2020) 10–16, https://doi.org/10.1016/j.mattod.2019.11.001.

[38] J. Lu, H. Lu, X. Xu, J. Yao, J. Cai, K. Luo, High-performance integrated additive manufacturing with laser shock peening –induced microstructural evolution and improvement in mechanical properties of ti6al4v alloy components, International Journal of Machine Tools and Manufacture 148. doi:10.1016/j.ijmachtools.2019.103475.

[39] P. Peyre, L. Berthe, V. Vignal, I. Popa, T. Baudin, Analysis of laser shock waves and resulting surface deformations in an al–cu–li aluminum alloy, J. Phys. D: Appl. Phys. 45 (33) (2012) 335304, https://doi.org/10.1088/0022-3727/45/33/335304.

[40] M. Ayad, L. Lapostolle, A. Rondepierre, C. Le Bras, M. Scius-Bertrand, S. Ünaldi, U. Trdan, Y. Rouchausse, J. Grassy, T. Maillot, V. Lapoujade, C. Michel, L. Berthe, Modeling of multi-edge effects in the case of laser shock loadings applied on thin foils: Application for material characterization of aluminum alloys, J. Appl. Phys. 131 (9) (2022) 095902, https://doi.org/10.1063/5.0080326.

[41] D.-N. Zhang, Q.-Q. Shangguan, C.-J. Xie, F. Liu, A modified johnson–cook model of dynamic tensile behaviors for 7075–t6 aluminum alloy, J. Alloy. Compd. 619 (2015) 186–194, https://doi.org/10.1016/j.jallcom.2014.09.002.

[42] Q. hua Lin, B. ming Li, Numerical simulation of dynamic large deformation and fracture damage for solid armature in electromagnetic railgun, Defence Technology 16 (2) (2020) 348–353. doi:10.1016/j.dt.2019.05.020.

[43] Online materials information resource-matweb, http://www.matweb.com, accessed 23 March 2021 (2021).

[44] P. Bao-jun, L. Min, Z. Kai, The characteristics study of debris cloud of the mesh shields under hypervelocity impact, Vol. 6, ESA, 2013, pp. 22–25.

[45] A.J. Wilkinson, T.B. Britton, Strains, planes, and ebsd in materials science, Mater. Today 15 (9) (2012) 366–376, https://doi.org/10.1016/S1369-7021(12)70163-3.

[46] G.R. Johnson, W.H. Cook, A constitutive model and data for metals, International Ballistics Society, Hague, 1983, p. 7.

[47] B. O'Toole, M. Trabia, R. Hixson, S.K. Roy, S. Pena, S. Becker, E. Daykin, E. MacHorro, R. Jennings, M. Matthes, Modeling plastic deformation of steel plates in hypervelocity impact experiments, Procedia Engineering 103 (December) (2015) 458–465, https://doi.org/10.1016/j.proeng.2015.04.060.

[48] M. Scius-Bertrand, L. Videau, A. Rondepierre, E. Lescoute, Y. Rouchausse, J. Kaufman, D. Rostohar, J. Brajer, L. Berthe, Laser induced plasma characterization in direct and water confined regimes: New advances in experimental studies and numerical modelling, Journal of Physics D: Applied Physics 54 (5). doi:10.1088/1361-6463/abc040.

[49] A. Rondepierre, S. Ünaldi, Y. Rouchausse, L. Videau, R. Fabbro, O. Casagrande, C. Simon-Boisson, H. Besaucéle, O. Castelnau, L. Berthe, Beam size dependency of a laser-induced plasma in confined regime: Shortening of the plasma release. Influence on pressure and thermal loading, Optics and Laser Technology 135 (November 2020). doi:10.1016/j.optlastec.2020.106689.

[50] Y. Chen, R. Zhang, C. He, F. Liu, K. Yang, C. Wang, Q. Wang, Y. Liu, Effect of texture and banded structure on the crack initiation mechanism of a friction stir welded magnesium alloy joint in very high cycle fatigue regime, Int. J. Fatigue 136 (2020) 105617, https://doi.org/10.1016/j.ijfatigue.2020.105617.

[51] H. Schmidt, T. Dickerson, J. Hattel, Material flow in butt friction stir welds in aa2024-t3, Acta Mater. 54 (4) (2006) 1199–1209, https://doi.org/10.1016/j.actamat.2005.10.052.

[52] S. Xu, X. Deng, A study of texture patterns in friction stir welds, Acta Mater. 56 (6) (2008) 1326–1341, https://doi.org/10.1016/j.actamat.2007.11.016.

[53] S. Sinhmar, D.K. Dwivedi, A study on corrosion behavior of friction stir welded and tungsten inert gas welded aa2014 aluminium alloy, Corros. Sci. 133 (2018) 25–35, https://doi.org/10.1016/j.corsci.2018.01.012.

[54] H. Schmidt, J. Hattel, J. Wert, An analytical model for the heat generation in friction stir welding, Modell. Simul. Mater. Sci. Eng. 12 (1) (2003) 143–157, https://doi.org/10.1088/0965-0393/12/1/013.

[55] R. Seddik, A. Rondepierre, S. Prabhakaran, L. Morin, V. Favier, T. Palin-Luc, L. Berthe, Identification of constitutive equations at very high strain rates using shock wave produced by laser, Eur. J. Mech. A. Solids 92 (2022) 104432, https://doi.org/10.1016/j.euromechsol.2021.104432.

[56] F. Plassard, J. Mespoulet, P. Hereil, Hypervelocity impact of aluminium sphere against aluminium plate: experiment and ls-dyna correlation, in: 8th European LS-DYNA Users Conference, DYNALOOK, 2011.

[57] J.A. Smith, J.M. Lacy, D. Lévesque, J.P. Monchalin, M. Lord, Use of the Hugoniot elastic limit in laser shockwave experiments to relate velocity measurements, AIP Conference Proceedings 1706 (February). doi:10.1063/1.4940537.

[58] P. Ballard, Contraintes résiduelles induites par impact rapide. Application au choc laser, PhD Thesis, Ecole Polytechnique (1991).

[59] J. Brunner, N. Birbilis, K. Ralston, S. Virtanen, Impact of ultrafine-grained microstructure on the corrosion of aluminium alloy aa2024, Corros. Sci. 57 (2012) 209–214, https://doi.org/10.1016/j.corsci.2011.12.016.

[60] W. Dou, B. Wang, X. Geng, J. Fan, Grain size effect on strain-rate dependence of mechanical properties of polycrystalline copper, Mater. Sci. Technol. 35 (11) (2019) 1401–1404, https://doi.org/10.1080/02670836.2019.1625527.